A study of the effects of the assumption of local-thermal equilibrium on the overall thermally-induced response of a decomposing, glass-filled polymer composite

JOHN FLORIO, JR.†

Kaman Sciences Corporation, AviDyne Division, 83 Second Avenue, Northwest Industrial Park,
Burlington, MA 01803, U.S.A.

and

JACK B. HENDERSON, FREDERICK L. TEST and
RAMAMURTHY HARIHARAN

Department of Mechanical Engineering and Applied Mechanics, University of Rhode Island,
Kingston, RI 02881, U.S.A.

Abstract—An analytical study is conducted to determine the thermal response of a widely used ablative glass-filled polymer composite. This study is performed using a newly developed one-dimensional, transient numerical model which does not include the idealized assumption of local-thermal equilibrium existing between the solid matrix and decomposition gases within the tortuous pore network of the material. Results of this study include solid temperature, decomposition gas temperature, solid mass loss, pressure, permeability, porosity, gas mass flux, gas mass storage, expansion and volumetric heat transfer coefficient profiles. Deviations from local-thermal equilibrium as high as 200°C are predicted. Pressures as high as 10 atm are predicted, and the existence of such high pressures is verified experimentally. An investigation into the effects of the idealized assumption of local-thermal equilibrium reveals significant errors associated with the assumption.

INTRODUCTION

POLYMER composites are currently used in a wide variety of structural and thermal protection applications. Although the structural applications of polymer composites have resulted in the bulk of research activities being concentrated on mechanics and mechanical properties, there has over the past decade been an increasing interest in the high-temperature, thermal protection application of these materials. In the area of glass-filled polymer composites, the impetus behind this recent interest has been their use in such high-temperature, thermal protection systems as spacecraft heat shields for re-entry, missile magazines, rocket motor nozzle liners and blast deflectors. In these applications, the materials are exposed to temperatures high enough to cause decomposition of the solid material. In fact, overwhelming acceptance of this material stems from a high char yield resulting from pyrolysis reactions, coupled with favorable thermal and transport properties of the product char. As a result of the decomposition process, the overall thermally induced response of the material is quite complex and varies with material composition and processing. To design reliable and efficient thermal protection systems, it is necessary to predict the thermally-induced response of these materials a priori. Accurate prediction of this thermal behavior requires the solution of a complex numerical model which includes all of the physical processes that occur in the material over the temperature range of interest. This response is, of course, governed in part, by the material properties which must be accurately determined and modeled so as to be used in the overall numerical scheme.

Although many excellent mathematical models exist for the prediction of the thermal response of these and other materials [1–4], to the best of the authors' knowledge there have been no in-depth analytical investigations dealing with the prediction of their overall response in the absence of local thermal equilibrium.

MATERIAL BEHAVIOR

When a polymer composite material is exposed to a surface heat flux, the initial heat transfer away from the surface is primarily due to transient energy conduction. This heat conduction is solely governed by

---

† Previously at the University of Rhode Island.

NOMENCLATURE

a	Nusselt–Reynolds correlation coefficient		**Greek symbols**	
A	pre-exponential factor		α	linear coefficient of thermal expansion
b	Nusselt–Reynolds correlation coefficient		β	inertial coefficient
			γ	permeability
C_p	specific heat		δ	decomposition porosity coefficient
E	activation energy		ΔA	cross-sectional area
F	mass fraction		Δx	control system width
h_t	volumetric heat transfer coefficient		ε	emissivity
H	specific enthalpy		ζ	decomposition permeability coefficient
k	thermal conductivity		η	heating rate expansion coefficient
L	specimen thickness		λ	generic variable
m	mass		μ	viscosity
$\dot{m}''$	mass flux		ξ	decomposition expansion coefficient
M	molecular weight of gases		ρ	density
n	order of reaction		Φ	porosity
P	pressure		Ψ	coefficient of linear permeability.
Q	heat of decomposition			
R	universal gas constant		**Subscripts**	
t	time coordinate		c	char
T	temperature		f	final
v	gas velocity		g	gas
U	specific enthalpy		s	solid
x	spatial coordinate.		v	virgin
			0	initial.

the thermal properties of the virgin material. During this period, the material experiences a small amount of expansion, characterized by the linear coefficient of the thermal expansion of the virgin material, i.e. α_v.

When the material reaches sufficiently high temperatures (200–300°C), dependent on material processing, composition and heating rate, chemical reactions begin to occur. These thermally-induced reactions, commonly referred to as pyrolysis reactions, result in the degradation of the resin component of the composite matrix to residue char and product volatiles. This reaction zone moves from the heated surface through the material. During the initial stages of the pyrolysis reactions, decomposition gases are trapped within the pore network due to low material permeability. This accumulation of gases results in the internal pressurization of the material. For many polymer composites the porosity and permeability are small enough to cause the internal pressure to become quite high.

The internal pressurization is at least partially responsible for a very rapid and sometimes quite large expansion of the material which occurs at this time. The work associated with expansion is now a means for energy transfer. As a result of the continuing expansion and decomposition, the material permeability and porosity begin to increase. This increased permeability, coupled with existing pressure gradients, results in the flow of gas through the pore

network. As a result, energy is transferred between the product gas and solid material within the pore network by means of forced convection. The rate at which energy is transferred between the two phases is characterized by the volumetric heat transfer coefficient, h_t. This highly transient energy transfer results in large deviations from thermal equilibrium existing locally between the two phases. The gases which flow back through the char structure remove energy by convection with the solid, thus attenuating the conduction of heat to the reaction zone. The gases which flow, in the other direction, through the partially virgin material serve to pre-heat the material. The rate of doing work resulting from the flow of gas now becomes an important means of energy transfer.

As the pyrolysis reactions and expansion proceed, the permeability and porosity of the material increase still further. This results in increased gas flow and in a reduction in internal pressure. When this occurs, the material experiences a rapid contraction, primarily due to elastic recovery, followed by a slower contraction which is characterized by the linear coefficient of thermal expansion of the char, α_c.

At temperatures in excess of 1000°C, the carbonaceous char reacts with silica, present in the glass fibers, resulting in considerable additional mass loss. However, there is no significant increase in the internal pressure as the permeability is large enough to allow the decomposition gases to flow freely out of the

material. Deviations from local thermal equilibrium may become quite large at this time due to high gas flow rates, limiting contact time between the phases. As a result of the degradation of the glass reinforcement, coupled with considerable solid mass loss, the material exhibits very severe contraction at this time. Given sufficient incident energy, the active material may entirely be consumed. The final products may include a combination of solid phase silicon carbide and product gases or an entirely gaseous phase.

MODEL DESCRIPTION

A one-dimensional transient mathematical model has been developed to predict the thermally induced response of a polymer composite matrix in the absence of thermal equilibrium. Since heat transfer is accompanied by fluid flow, it was necessary to require the conservation of thermal energy, momentum and mass in the system. Additionally, thermochemical expansion, solid matrix decomposition and temperature-dependent property relations were included in the overall modeling scheme. The major simplifying assumptions incorporated into the model were that decomposition gases behave ideally and are inert, and that the specific internal energy of the solid is equivalent to the specific enthalpy of the solid.

The introduction of convective thermal transport between the solid and volatiles requires that separate energy equations be derived for each phase. An energy balance was applied over a non-stationary volume element, $\Delta A \Delta x$, to obtain the equations of energy for both the solid and gas phases. Δx represents the instantaneous control system width. These equations of energy are non-linear, coupled partial differential equations that describe the conservation of energy in the fluid or the solid phase. The following equations constitute the mathematical description for energy conservation in the overall model:

$$\frac{\partial}{\partial t}(m_s U_s) = \Delta A \Delta x \frac{\partial}{\partial x}\left[k_s(1-\Phi)\frac{\partial T_s}{\partial x}\right]$$

$$+ h_r \Delta A \Delta x(T_g - T_s) + P\Phi\Delta A \frac{\partial \Delta x}{\partial t}$$

$$- Q\frac{\partial m_s}{\partial t} + H_g(T_s)\frac{\partial m_s}{\partial t} \quad (1)$$

$$\frac{\partial}{\partial t}[(\rho_g U_g + \tfrac{1}{2}\rho_g v^2)\Delta A \Delta x \Phi] = \Delta A \Delta x \frac{\partial}{\partial x}\left(k_g \Phi \frac{\partial T_g}{\partial x}\right)$$

$$- \Delta A \Delta x \frac{\partial}{\partial x}[(\rho_g U_g + \tfrac{1}{2}\rho_g v^2)\Phi v]$$

$$+ h_r \Delta A \Delta x(T_s - T_g) - P\Phi\Delta A \frac{\partial \Delta x}{\partial t}$$

$$- \Delta A \Delta x \frac{\partial (P\Phi v)}{\partial x} - H_g(T_s)\frac{\partial m_s}{\partial t}. \quad (2)$$

Equation (1) describes the transport of energy within the solid phase. The first term in this equation represents the accumulation of internal energy within the control system, $\Delta A \Delta x$; the second term represents the net rate of energy transfer by conduction; the third term represents the rate of energy transferred by convection between the solid material and volatiles, characterized by the volumetric heat transfer coefficient, h_r; the fourth term accounts for the rate of work of expansion; the fifth term depicts energy consumption/generation during chemical reactions; the last term accounts for the energy lost by the flow of newly generated product gas from the solid matrix into the gas stream, i.e. pore network.

Equation (2) describes the transport of energy within the gas phase. The first term in this equation represents the accumulation of internal and kinetic energy; the second term represents the net rate of energy transfer by conduction within the gas phase; the third term represents the net rate of convection of internal and kinetic energy solely within the gas phase; the sixth term depicts the rate of doing work against the static pressure, P, at the control system faces, i.e. flow work.

The appropriate form of the equation of continuity was obtained by writing a mass balance over the non-stationary volume element, $\Delta A \Delta x$. The result being

$$\frac{\partial m_g}{\partial t} = \frac{\partial m_s}{\partial t} - \Delta A \Delta x \frac{\partial \dot{m}_g''}{\partial x}. \quad (3)$$

The first term in equation (3) represents the rate of gas mass accumulation; the second term accounts for the rate of solid mass decomposition, i.e. gas generation; the last term accounts for the net rate of mass flow in the control system. Momentum conservation is modeled using a non-Darcy type correlation, governing flow through porous media. That is

$$-\frac{\partial P}{\partial x} = \frac{\mu_g}{\rho_g \gamma}\dot{m}_g'' + \frac{\beta \dot{m}_g''}{\rho_g}|\dot{m}_g''| \quad (4)$$

where $\beta = c_s/\gamma$. The first term on the right-hand side of equation (4) represents the contribution from Darcy's law; the last term accounts for departures from Darcy flow, primarily due to inertial effects, i.e. separation and/or turbulence.

The rate of solid mass decomposition is calculated by an nth order kinetic rate equation of the form

$$\frac{1}{m_0}\frac{\partial m_s}{\partial t} = -A\left(\frac{m_s - m_0}{m_f}\right)^n e^{[-E/RT_s]}. \quad (5)$$

The theoretical expansion of the control system, Δx, is modeled by an equation similar to that used by Henderson and Wiecek [4]

$$\frac{1}{\Delta x}\frac{\partial \Delta x}{\partial t} = \alpha_v F\frac{\partial T_s}{\partial t} + \alpha_c(1-F)\frac{\partial T_s}{\partial t} + \frac{\partial}{\partial t}\left(\eta T_s + \xi \frac{m_s}{m_0}\right). \quad (6)$$

The first and second terms of the right-hand side of equation (6) depict the linear thermal expansion of the virgin and char material, respectively; the last

term accounts for the contribution from the heating rate and decomposition process on the overall expansion behavior of the material.

The permeability, γ, and porosity, Φ, are given as follows [5, 6]:

$$\frac{1}{\gamma_0}\frac{\partial \gamma}{\partial t} = \Psi_c(1-F)\frac{\partial T_s}{\partial t} + \frac{\zeta}{m_0}\frac{\partial m_s}{\partial t} \qquad (7)$$

$$\frac{1}{\Phi_0}\frac{\partial \Phi}{\partial t} = \frac{\delta}{m_0}\frac{\partial m_s}{\partial t} \qquad (8)$$

respectively.

The instantaneous mass fraction of the virgin material is given by the following:

$$F = \frac{m_s - m_f}{m_0 - m_f}.$$

The ideal gas equation of state is used to specify the following relationship between the variables of state, that is:

$$P = \frac{m_g R T_g}{M \Phi \Delta A \Delta x}. \qquad (9)$$

The relation between specific heat and enthalpy for both phases is given by the following:

$$dH_s = C_{p_s}\,dT_s \qquad (10)$$

$$dH_g = C_{p_g}\,dT_g \qquad (11)$$

$$H_s = \int_{T_0}^{T_s} C_{p_s}\,dT \qquad (12)$$

$$H_g = \int_{T_0}^{T_g} C_{p_g}\,dT \qquad (13)$$

$$H_g(T_s) = \int_{T_0}^{T_s} C_{p_g}\,dT. \qquad (14)$$

Lastly, the solid thermal conductivity, specific heat and surface emissivity were determined by weighted averages of virgin and char material. That is [4]

$$\lambda = \lambda_v F + (1-F)\lambda_c \qquad (15)$$

where

λ = generic variable representing the aforementioned properties.

The final form of the solid thermal energy equation used in the numerical scheme was obtained by substituting the approximation $H_s = U_s$ into equation (1), and then introducing equation (10) into the resultant expression. This yields

$$m_s C_{p_s}\frac{\partial T_s}{\partial t} = \Delta A \Delta x \frac{\partial}{\partial x}\left[k_s(1-\Phi)\frac{\partial T_s}{\partial x}\right]$$

$$+ h_r \Delta A \Delta x(T_g - T_s) + P\Phi \Delta A \frac{\partial \Delta x}{\partial t}$$

$$- \frac{\partial m_s}{\partial t}[H_s - H_g(T_s) + Q]. \qquad (16)$$

Note that Q is a negative quantity for endothermic reactions.

The final form of the gas thermal energy equation used in the numerical scheme is obtained by substituting the appropriate form of the mechanical energy equation into equation (2), and then introducing equation (3) into the resulting expression. This yields

$$m_g C_{p_g}\frac{\partial T_g}{\partial t} = \dot{m}_g''\Delta A \Delta x C_{p_g}\frac{\partial T_g}{\partial x}$$

$$+ \Delta A \Delta x \frac{\partial}{\partial x}\left(k_g \Phi \frac{\partial T_g}{\partial x}\right) + h_r \Delta A \Delta x(T_s - T_g)$$

$$+ \Delta A \Delta x \frac{D(\Phi P)}{Dt} - \frac{\partial m_s}{\partial t}[-H_g + H_g(T_s) + v^2/2]. \qquad (17)$$

The volumetric heat transfer coefficient, h_v, is calculated based on the following correlation [7]:

$$Nu = a\,Re^b \qquad (18)$$

$$Nu\frac{h_r\gamma}{k_g} \qquad (19)$$

$$Re = -\frac{\rho_g \gamma^{1.5}}{\mu_g^2 \Phi}\frac{\partial P}{\partial x}. \qquad (20)$$

Equations (16), (17) and (3)–(8) represent a set of coupled, non-linear partial differential equations in T_s, T_g, $\dot{m}_g''$, P, m_s, Δx, γ and Φ, respectively. In the numerical scheme, this set of governing equations was approximated using a fully implicit finite-difference technique. All time derivatives were approximated using a forward difference technique with a local truncation error of the order of Δt, i.e. $O(\Delta t)$. All spatial derivatives were approximated by a central difference technique with a local truncation error $O(\Delta x^2)$, with the exception of the boundary nodes where local truncation errors on spatial derivatives were $O(\Delta x)$. The above uncertainty analysis is worthwhile because it allows for the comparison of the local accuracies of various differencing schemes. A more detailed description of the model is presented elsewhere [8].

MATERIAL

The composite studied is designated as H41N, fabricated by Ametek Haveg Division. The resin is of the thermosetting variety, undergoing chemical crosslinking during fabrication. The result is an infusible, insoluble, three-dimensional structure. This material consists of 39.5% phenol-formaldehyde resin and 60.5% glass and talc filler. The fiberglass (reinforcing material) may contain coupling agents and binders to insure proper adhesion to the resin network. The fillers improve both the impact strength and flexural modulus of the composite. This material was chosen for study because it exhibits typical decomposition/length change behavior for glass-filled thermoset composites. This material is also of a great

practical importance since it is used extensively in high-temperature, high-heating rate thermal protection applications.

The manufacturing procedure consists of mixing the glass fibers and talc into the resin, such that the glass fibers are randomly orientated. The material is then placed in a mold, and is either rolled or pressed until its shape conforms to that of the mold. During this procedure the glass fibers become partially orientated in a direction normal to the applied pressure. Afterwards, the material is cured in an autoclave at a specified pressure, under a carefully monitored heating cycle. As a result of this curing process, H41N exhibits somewhat transversely isotropic behavior. For example, the material expands significantly in the direction normal to the preferred fiber orientation, while displaying little expansion in other directions.

MATERIAL PROPERTIES

The accurate modeling of the overall thermally-induced response of these materials requires the accurate modeling of all of the chemical and physical pro-

cesses that occur over the temperature range of interest. The properties and modeling parameters for H41N are listed in Table 1. The properties of the product gas are listed in Table 2. In both tables, mass loss or temperature ranges are specified over which the modeling parameter or function is applicable. With the exception of permeability, porosity, expansion and volumetric heat transfer coefficient data, all of the properties and parameters listed in Tables 1 and 2 were assembled from a study performed by Henderson and Wiecek [4]. Permeability and porosity data and corresponding parameters were taken from more recent studies by Ramamurthy [5] and Doherty [6], respectively. While volumetric heat transfer coefficient data and corresponding parameters were taken from an experimental study performed by Florio et al. [7]. The expansion data were obtained from an experimental study performed by Florio et al. [9].

RESULTS AND DISCUSSION

Using the appropriate equations and thermal property relations outlined earlier, the thermally-induced

Table 1. Material properties for H41N

Property/parameter	Function†	Range†
ρ_v (kg m^{-3})	1810.0	
k_v (W m^{-1} K^{-1})	$0.80+2.76\times10^{-4}\,T$	$20 \leqslant T \leqslant 1000$
k_c (W m^{-1} K^{-1})	$0.96+8.42\times10^{-4}\,T$	$20 \leqslant T \leqslant 1000$
	$-4.07\times10^{-6}\,T^2+5.32\times10^{-9}\,T^3$	
C_{pv} (kJ kg^{-1} K^{-1})	$1.05+9.76\times10^{-4}\,T$	$20 \leqslant T \leqslant 1200$
C_{pc} (kJ kg^{-1} K^{-1})	$0.88+7.60\times10^{-4}\,T$	$20 \leqslant T \leqslant 1200$
Φ_v (—)	0.113	
Φ_c (—)	0.274	
δ (—)	-0.866	$m_s/m_0 \leqslant 1$
γ_v (m^2)	6.18×10^{-18}	
γ_c (m^2)	4.85×10^{-15}	
Ψ_v (K^{-1})	0	
Ψ_c (K^{-1})	0	
ζ (—)	-2619.0	$0.795 \leqslant m_s/m_0 \leqslant 0.99$
c	0	
α_v (K^{-1})	8.59×10^{-5}	
α_c (K^{-1})	-7.42×10^{-5}	$0.492 < m_s/m_0 \leqslant 0.99$
	-5.93×10^{-4}	$m_s/m_0 = 0.492$
η (K^{-1})	8.03×10^{-4}	$0.92 \leqslant m_s/m_0 \leqslant 0.99$
	-1.68×10^{-4}	$0.81 \leqslant m_s/m_0 < 0.92$
ξ (—)	0.967	$0.92 \leqslant m_s/m_0 \leqslant 0.99$
	0.445	$0.81 \leqslant m_s/m_0 < 0.92$
	-2.19×10^{-2}	$0.492 \leqslant m_s/m_0 < 0.795$
A (s^{-1})	1.98×10^{29}	$m_s/m_0 \geqslant 0.91$
	8.17×10^{18}	$0.795 \leqslant m_s/m_0 > 0.91$
	2.62×10^{7}	$m_s/m_0 \geqslant 0.795$
E (kJ kmol^{-1})	2.60×10^{5}	$m_s/m_0 \geqslant 0.795$
	3.54×10^{5}	$m_s/m_0 < 0.795$
n (—)	17.33	$m_s/m_0 \geqslant 0.91$
	6.30	$0.795 \leqslant m_s/m_0 < 0.91$
	0.53	$m_s/m_0 < 0.795$
Q (kJ kg^{-1})	-234.0	$m_s/m_0 \geqslant 0.795$
	-2093.0	$m_s/m_0 < 0.795$
ε_v	0.84	
ε_c	0.88	
a	2.22×10^{-6}	$m_s/m_0 \geqslant 1$
b	0.703	$m_s/m_0 \geqslant 1$

† Temperature in °C.

Table 2. Decomposition gas properties

Property/parameter	Function†	Range†
k_g (W m^{-1} K^{-1})	$0.03 + 1.40 \times 10^{-4}\, T$	$20 \leqslant T \leqslant 1000$
C_{pg} (kJ kg^{-1} K^{-1})	$2.39 + 1.05 \times 10^{-3}\, T$	$20 \leqslant T \leqslant 1000$
μ_g (kg m^{-1} s^{-1})	$1.48 \times 10^{-5} + 2.50 \times 10^{-8}\, T$	$20 \leqslant T \leqslant 1000$
M (kg kmol^{-1})	18.35	

† Temperature in °C.

response of H41N was evaluated. The model was exercised for a 0.03 m thick slab with a radiant heat flux of 279.7 kW m^{-2} applied to the front boundary, $x = 0$. The back boundary, $x = L$, was prescribed to be insulated. The pressure at both boundaries was fixed at 1.01325×10^5 Pa (1 atm). The initial temperature and pressure were taken as 40°C and 1.01325×10^5 Pa, respectively. These boundary and initial value conditions were prescribed to simulate conditions under which actual experiments were to be conducted.

For H41N, the computer simulation run was made utilizing 151 nodes and a time step of 0.2 s. It was determined that further reduction in the number of nodes or in the time step altered the results by less than 1%.

The accuracy of the model was established by comparing predicted and experimental solid temperature and gas pressure profiles for H41N. The experimental temperature and pressure profiles were obtained from a study performed by Ramamurthy et al. [10] for the same initial and boundary value conditions, and sample geometry as used in the numerical scheme.

These researchers implanted thermocouples in the material at known initial depths in order to record solid temperature data. Experimental uncertainty in the solid temperature measurements was given as ±5%. The measurement of internal gas pressure was

performed by inserting hypodermic tubing into the material, and sealing the tube with a ceramic cement so gas could not escape. A miniature strain gage was fixed on the free end of each tube, and the pressure which developed in the material during decomposition was recorded as a voltage corresponding to a deflection of the strain gage. For H41N, solid temperature and gas pressure readings were taken in the same sample.

Figure 1 shows a comparison of analytical and experimental solid temperature profiles as a function of time for initial depths of 0.1, 1.0 and 2.9 cm. Evident from this figure is the relatively good agreement between analysis and experiment.

Analytical and experimental gas pressure profiles are compared in Fig. 2, as a function of time for a depth of 0.6 cm. There appears to be excellent agreement between the peak analytical and experimental pressures, with peaks of 9 and 9.7 atm, respectively. However, the experimental pressure drops off very rapidly after the peak value. These researchers attribute this behavior to poor cement bonding between the hypodermic tubing and the specimen, magnified by differences in the expansion characteristics of the cement and specimen. Consequently, cracks develop at the interface resulting in leakage of gas. They conclude that as a result of experimental difficulties, the internal gas pressure is at least as high as the recorded
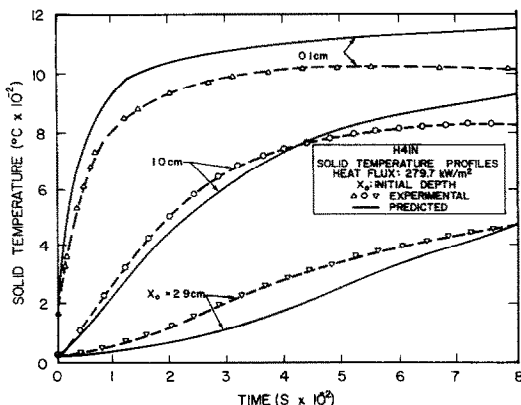

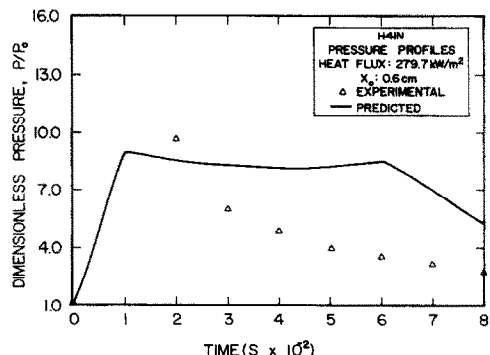FIG. 1. Comparison of predicted and experimental solid temperature profiles for H41N.

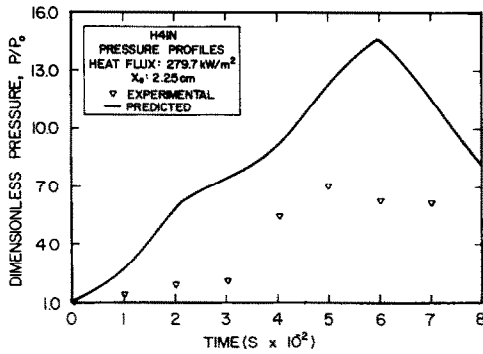FIG. 2. Comparison of predicted and experimental pressure profile at 0.6 cm for H41N.

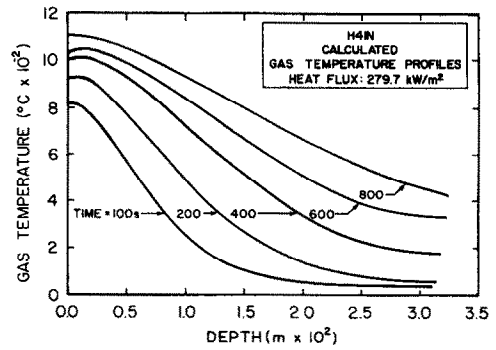FIG. 3. Comparison of predicted and experimental pressure profiles at 2.25 cm for H41N.

FIG. 5. Gas temperature profiles for H41N.

pressure. Figure 3 shows the analytical and experimental pressure profiles as a function of time for a depth of 2.25 cm. The peak analytical and experimental pressure are approximately 14.5 and 7.0 atm, respectively. In fact, for all this, the experimental data are well below the analytical. In both Figs. 2 and 3, the fact that the peak value of P/P_0 occurs at about the same time for both analysis and experiment is encouraging.

The thermally induced response of H41N as a function of time and depth is shown in Figs. 4–13. All profiles are shown at times of 100, 200, 400, 600 and 800 s.

Figure 4 illustrates the temperature history of the solid material for H41N. Evident from this figure are the steep temperature profiles, present primarily because of the low solid thermal conductivity. Also evident is the expansion of the material, as each successive time curve ends further beyond the previous one. By 800 s, the material has expanded from an initial thickness of 0.03 m to approximately 0.032 m.

Figure 5 illustrates the temperature history of the product gas for H41N. A comparison of Figs. 4 and 5 shows large differences between the two temperature

profiles. In fact, deviations from local thermal equilibrium as high as 200°C are predicted. Note that for a particular time, the major deviation from thermal equilibrium occurs at the front surface. This is expected because this surface is exposed to the radiant heat flux, and thus subject to rapid heating. However, this deviation from thermal equilibrium decreases with increasing time due to the balancing of absorbed energy with emitted energy at the solid surface, i.e. solid surface temperature approaching a uniform value.

Figure 6 shows the mass loss history for H41N. The ordinate axis represents the fraction of mass remaining, $m_s/m_{s,0}$. For H41N, the pyrolysis reactions result in a mass loss of about 20%, i.e. $m_s/m_{s,0} = 0.8$. A comparison of Figs. 4 and 6 shows that the pyrolysis reactions are initiated in the solid temperature range of approximately 350–375°C, and reach completion in the solid temperature range of approximately 1000–1100°C. As a result, it is evident from Fig. 6 that the reactions have reached completion at the heated surface for times greater than 100 s, and by 800 s the reaction zone has progressed to the back surface. Also evident from this figure is the fact that the radiant heat flux of 279.7 kW m^{-2} does not apply sufficient
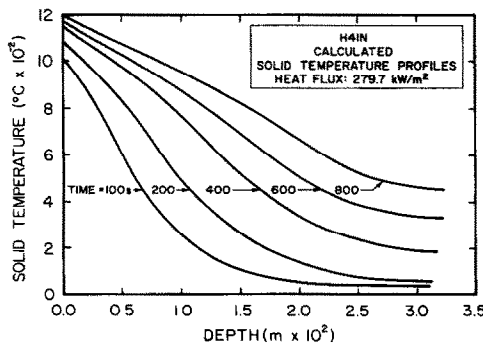

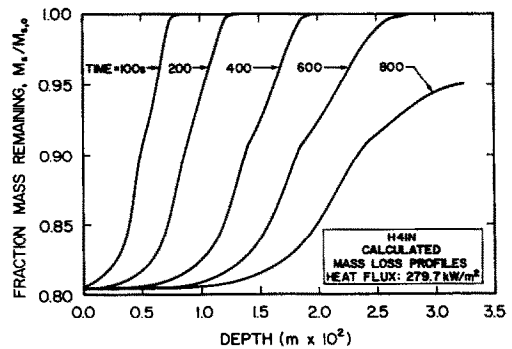FIG. 4. Solid temperature profiles for H41N.
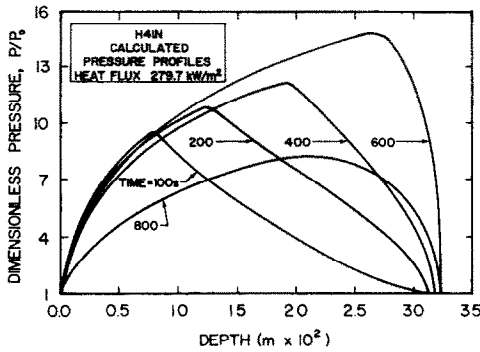

FIG. 6. Mass loss profiles for H41N.

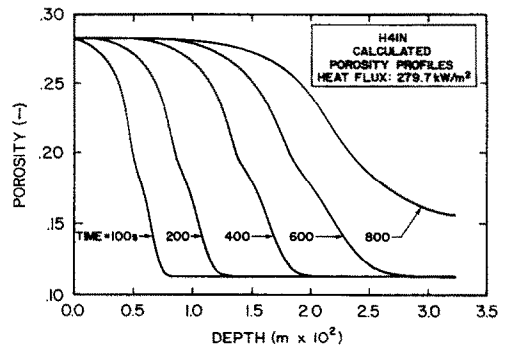FIG. 7. Pressure profiles for H41N.

FIG. 9. Porosity profiles for H41N.

incident energy for the initiation of the carbon–silica reactions in this material which occur when $m_s/m_{s,0} < 0.8$.

The dimensionless pressure, p/p_0, profiles for H41N are shown in Fig. 7. As can be seen the peak pressure moves further into the material with increasing time, following the pyrolysis reaction zone. A comparison of Figs. 6 and 7 shows that for a given time the peak pressure takes place just after the onset of pyrolysis $(m_s/m_{s,0} < 0.98)$, primarily due to low material permeability and porosity in this region. The permeability and porosity profiles are shown in Figs. 8 and 9, respectively. The sole exception to this is at 800 s, where as discussed earlier the pyrolysis zone has progressed through the material. As a result, Fig. 8 reveals that the material permeability at the back surface has become quite large by 800 s. Hence, the gas can flow quite freely out the back surface, resulting in a reduction in the entire pressure field.

Figure 10 shows the decomposition gas mass flux, m_g'', profiles through the material. A negative value on the ordinate axis indicates flow towards the heated surface, while a positive value indicates flow towards the back surface. As expected from the above discussion the majority of the decomposition gas exits the material by way of the heated surface, except at

800 s where appreciable flow out the back surface occurs. Also a comparison of Figs. 7 and 10 indicates that the peak pressure for a given time occurs with the initiation of gas flow towards the heated surface. This, of course, is expected behavior, based on equation (4).

The ratio of the instantaneous decomposition gas mass storage to the initial gas mass occupying the pores, $m_g/m_{g,0}$, is depicted in Fig. 11. Comparison of Figs. 6 and 11 reveals that the peak gas storage occurs midway in the pyrolysis reaction region. Secondary plateaus are also seen in Fig. 11 within the virgin material, where no mass loss has occurred. These plateaus are created as a result of gas flow towards the back surface. This gas becomes trapped due to the low material permeability in this region. A comparison of Figs. 8 and 11 reveals that the secondary plateaus do indeed begin where the permeability is essentially zero. A secondary plateau is not present on the profile at 800 s due to a high permeability at the back surface. A comparison of Figs. 10 and 11 reveals that the peak gas mass storage lags the peak pressure. The peak pressure actually occurs in the secondary plateau region as a result of the small volume available for gas storage, $\Phi \Delta x \Delta A$, associated with the virgin material in this region.
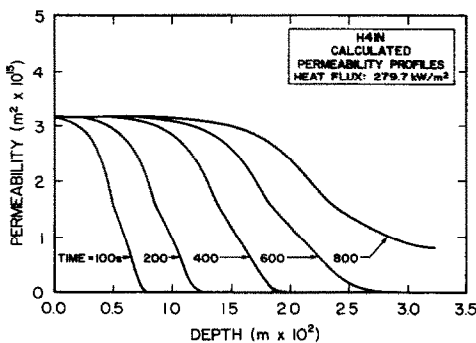

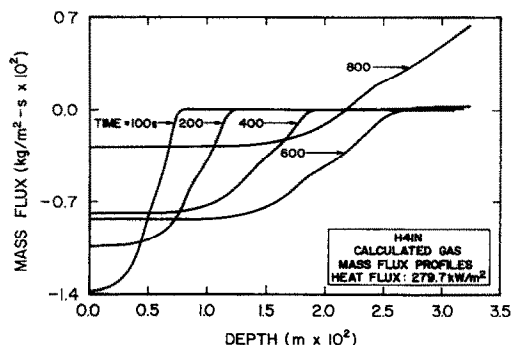FIG. 8. Permeability profiles for H41N.
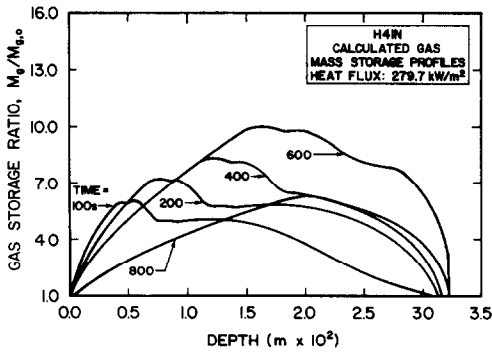

FIG. 10. Gas mass flux profiles for H41N.

FIG. 11. Gas mass storage profiles for H41N.

FIG. 13. Volumetric heat transfer coefficient profiles for H41N.

The expansion profiles for H41N are shown in Fig. 12. The fractional length change, $(\Delta x - \Delta x_0)/\Delta x_0$, is represented on the ordinate axis. Inspection of the figure clearly reveals the distinct stages of expansion described earlier. As can be seen, expansion as high as 15% occurs as a result of pyrolysis. Clearly, this is significant, and has a direct impact on the overall response of the material. As with pressure, expansion follows the pyrolysis zone, moving further into the material with increasing time. However, examination of Figs. 7 and 12 shows that the peak expansion lags the peak pressure for a given time. The peak expansion actually occurs midway in the pyrolysis reactions. This is thought to occur because the char material in the pyrolysis region has a much lower specific strength than the virgin material. Hence, the char structure is weaker, allowing for more expansion as a result of internal pressurization. Another interesting point is that peak expansion coincides with peak gas storage. The volume increase associated with this large expansion and high porosity was presented earlier as the reason the peak value of $m_g/m_{g,0}$ and peak pressure do not coincide. A more detailed discussion of the expansion characteristics of these materials is presented elsewhere [9].
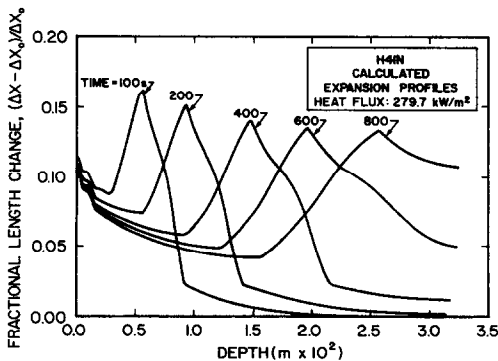
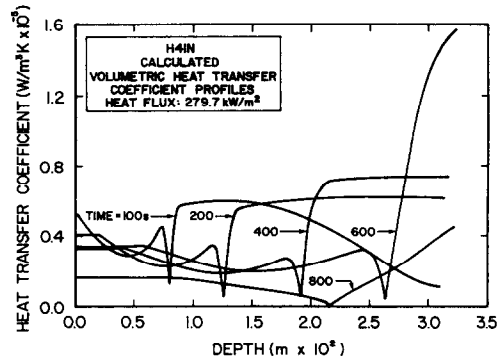Figure 13 illustrates volumetric heat transfer coefficient, h_v, profiles between decomposition gases and the solid within the pore network of the H41N. As expected from equation (18), the peak value of h_v for a given time occurs where the pressure gradient is steepest. Comparison of Figs. 13 and 7 shows that there is a sharp change in the volumetric heat transfer coefficient profile corresponding to the occurrence of the peak pressure. This phenomenon does not occur at 800 s, because the pressure profile is much flatter than at the earlier time. However, at 800 s, h_v approaches zero at a depth of about 2.2 cm due to a zero pressure gradient at this location.

The sensitivity of the overall response of this material to the various input parameters listed in Table 1 is presented in great detail elsewhere [11].

NON-THERMAL VS LOCAL-THERMAL EQUILIBRIUM

To determine the effects of the assumption of local-thermal equilibrium, the model was exercised for the same boundary conditions and sample geometry as in the earlier computer simulation run, i.e. Figs. 4–13. However, the volumetric heat transfer coefficient was fixed at 1.0×10^6 W m^{-3} K^{-1} throughout the solution domain. This value of the volumetric heat transfer coefficient induced approximate local-thermal equilibrium, with solid to gas temperature differences locally never exceeding 2% for all of the times investigated. This value of h_v is essentially two orders of magnitude greater than the actual values of h_v for H41N used to predict the actual thermal behavior of this material shown in Figs. 4–13 [7].

A comparison of the thermal response of H41N in local-thermal equilibrium and in the absence of local-thermal equilibrium is shown in Figs. 14–22 as a function of depth for times of 400 and 800 s. In each figure the dashed lines represent the profile corresponding to the case of local-thermal equilibrium from this computer simulation run. The solid line corresponds to a case of non-thermal equilibrium generated from the earlier computer simulation run using equation (18),
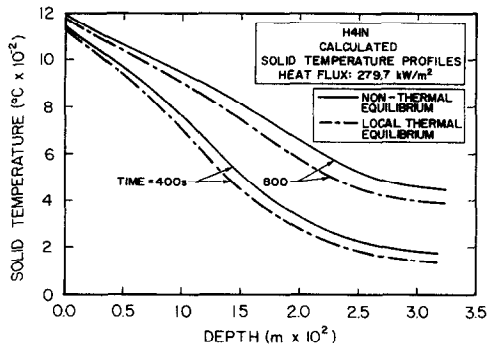

FIG. 12. Expansion profiles for H41N.

FIG. 14. Comparison of non-thermal equilibrium and local-thermal equilibrium solid temperature profiles.

FIG. 16. Comparison of non-thermal equilibrium and local-thermal equilibrium mass loss profiles.

which is correlated to experimentally determined values of h_c.

Figure 14 shows the solid temperature profiles. Clearly, significant differences exist between the cases of non-thermal and local-thermal equilibrium. Also evident from this figure is that the system in non-thermal equilibrium has higher solid temperatures throughout the solution domain. This is expected since the system in local-thermal equilibrium transfers much more energy to the product gas to induce thermal equilibrium, especially at the heated surface. Remember for the most part energy transfer is from the solid to the gas since the majority of the product gas flows towards the heated surface. Observation of this figure also reveals that the difference between the two cases increases with time. This is due to the highly transient nature of the system. That is, the total amount of additional energy retained by the solid phase for the system in non-thermal equilibrium increases with increasing time, resulting in a greater temperature difference between the two cases with increasing time.

Figure 15 shows the gas temperature profiles. As with the solid temperature profiles, large differences exist between the two cases. As expected from earlier
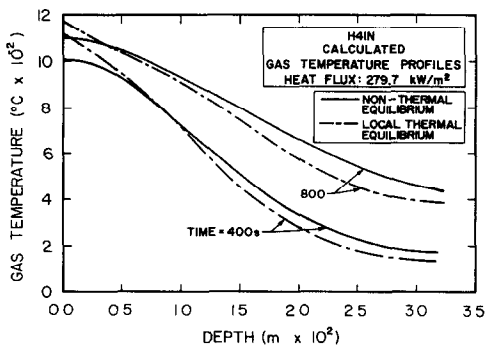
discussion, the gas temperatures near the front/heated surface are much lower for the system in non-thermal equilibrium. However, deeper into the material the gas temperatures for the system in non-thermal equilibrium become higher than those of the system in local-thermal equilibrium, primarily due to the corresponding significantly higher solid temperatures in this region, illustrated in Fig. 14. The differences between the gas temperature profiles for the two cases increase with time following the differences in the solid temperature profiles.

Figure 16 shows the mass loss profiles. Inspection of this figure reveals that the pyrolysis decomposition zone progressed further into the material for the system in non-thermal equilibrium, and that the difference between the two cases is enhanced with increasing time, i.e. from 400 to 800 s. This behavior is expected since the pyrolysis reactions are solid temperature dependent, and the system in non-thermal equilibrium has the much higher temperatures throughout. Consequently, for a given depth, the pyrolysis reactions are initiated and completed at earlier times for the system in non-thermal equilibrium. Since material strength is highly dependent on stage of decomposition, the enhanced decomposition associated with the actual

FIG. 15. Comparison of non-thermal equilibrium and local-thermal equilibrium gas temperature profiles.

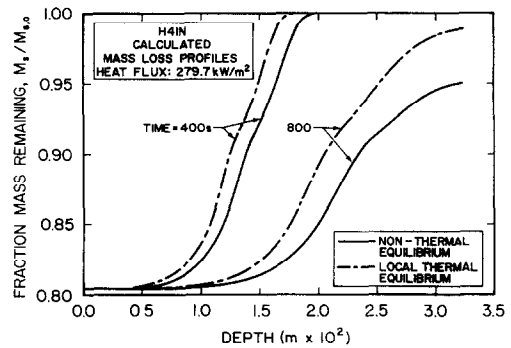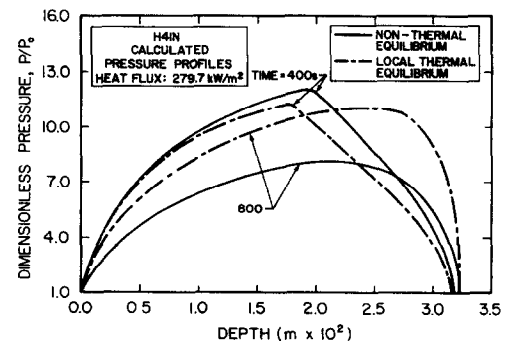FIG. 17. Comparison of non-thermal equilibrium and local-thermal equilibrium pressure profiles.
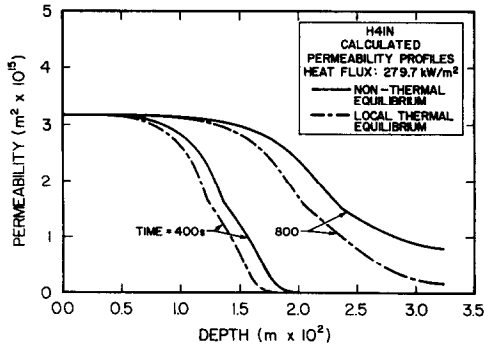
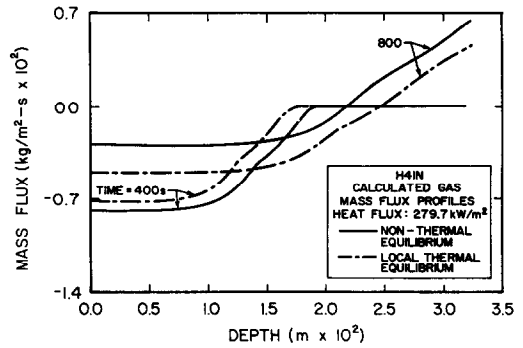FIG. 18. Comparison of non-thermal equilibrium and local-thermal equilibrium permeability profiles.

FIG. 20. Comparison of non-thermal equilibrium and local-thermal equilibrium gas mass flux profiles.

case/non-thermal equilibrium will strongly influence material failure. This indicates that accurate modeling of the thermal behavior of this material cannot be satisfactorily accomplished using the idealized assumption of local-thermal equilibrium.

The gas pressure profiles are shown in Fig. 17. At 400 s, the peak pressure is located further within the material for the system in non-thermal equilibrium. This is expected since the corresponding pyrolysis decomposition zone has progressed further into the material. The relationship between peak pressure and pyrolysis was presented earlier in the discussion of Fig. 4. Also at 400 s, the peak pressure is about 10% greater for the system in non-thermal equilibrium. This is a result of the increased resistance to gas flow as the pyrolysis reactions progress further into the material. However, by 800 s, the permeability and porosity at the back surface have become much larger for the system in non-thermal equilibrium due to enhanced decomposition. Consequently, the internal pressurization of the system in non-thermal equilibrium has been reduced and becomes much lower than the system in local-thermal equilibrium. The permeability and porosity profiles are shown in Figs. 18 and 19, respectively. The gas mass flux profiles are

depicted in Fig. 20. As expected from the discussion on the pressure field, the gas mass flux out the back surface is greater for the system in non-thermal equilibrium at 800 s.

The gas mass storage profiles are illustrated in Fig. 21. As expected, the differences in the two cases follow the difference in pressure behavior. The expansion profiles are shown in Fig. 22. As with decomposition and pressure, the expansion zone progresses more rapidly into the material for the system in non-thermal equilibrium. Also evident from this figure is the larger expansion at the back surface for the system in non-thermal equilibrium, associated with the enhanced decomposition.

CONCLUDING REMARKS

The numerical model developed during this study was used to quantify the overall thermally-induced response of a glass-filled polymer composite for a given set of boundary conditions. It has been demonstrated that glass-filled polymer composites exhibit complex thermal behavior when heated to high temperatures.

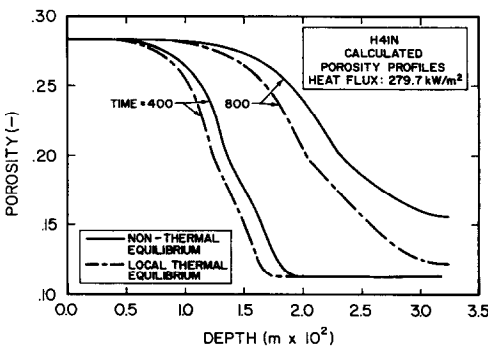The results of the initial simulation run with a pre-

FIG. 19. Comparison of non-thermal equilibrium and local-thermal equilibrium porosity profiles.
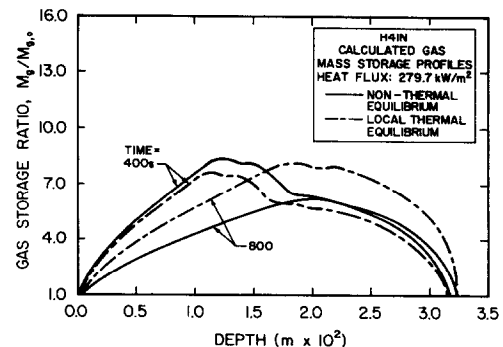

FIG. 21. Comparison of non-thermal equilibrium and local-thermal equilibrium gas mass storage profiles.
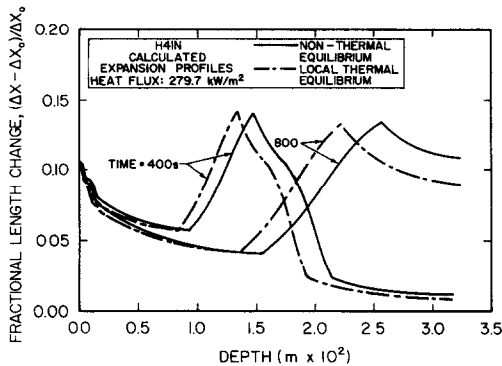
FIG. 22. Comparison of non-thermal equilibrium and local-thermal equilibrium expansion profiles.

scribed surface heat flux of 279.7 kW m^{-2} indicate that local thermal equilibrium does not exist in H41N. In fact, solid to gas temperature differences as high as 200°C exist locally. Pressures in excess of 10 atm were predicted, and the existence of such high pressures has been verified experimentally.

An investigation into the effects of the idealized assumption of local-thermal equilibrium revealed significant errors in predicted thermal behavior associated with the assumption. Solid temperature differences between the actual and idealized cases were as high as 100°C locally for H41N. The error associated with this difference is about 17%. As expected the solid temperature profiles are lower for the idealized case, due to increased heat transfer with the gas required to induce local-thermal equilibrium.

Due to the lower solid temperatures associated with the idealized case predicted decomposition severely lags that of the actual case. Measurable errors are evident in the mass loss profiles. As a result, the internal pressure profiles for the two cases differ in magnitude and are shifted further into the material for a given time for the system in non-thermal equilibrium, i.e. actual case. The errors in the pressure and mass loss profiles associated with the idealized case are significant because spallation and/or cracking are highly dependent on the stress concentration and specific strength of the material which are linked to the internal pressure and stage of decomposition, respectively. That is to say that internal pressurization and stage of decomposition define the failure of the material locally. From this discussion, and the results of this

study, it can be seen that accurate modeling of the overall thermal response of these types of materials, under similar boundary value conditions, can only be achieved when the idealized assumption of local-thermal equilibrium is not incorporated into the modeling scheme.

REFERENCES

1. H. C. Kung, A mathematical model of wood pyrolysis, *Combust. Flame* **18**, 185–195 (1972).
2. E. J. Kansa, H. E. Perlee and R. F. Chaiken, Mathematical model of wood pyrolysis including internal forced convection, *Combust. Flame* **29**, 311–324 (1977).
3. G. T. Boyer and W. C. Thomas, An analytical investigation of charring composites undergoing thermochemical expansion, *ASME Natn. Heat Transfer Conf.*, Denver, Colorado, Paper 85-HT-54 (August 1985).
4. J. B. Henderson and T. E. Wiecek, A numerical study of thermally-induced response of decomposing, expanding polymer composites, *Wärme- und Stoffübertr.* **22**, 275–284 (1988).
5. H. Ramamurthy, An experimental investigation into the thermophysical properties of decomposing polymer composites, M.S. Thesis, University of Rhode Island, Kingston, Rhode Island (1988).
6. M. P. Doherty, Characterization of the porous microstructure of decomposing glass-filled polymer composites, M.S. Thesis, University of Rhode Island, Kingston, Rhode Island (1988).
7. J. Florio, Jr., J. B. Henderson and F. L. Test, Experimental determination of volumetric heat transfer coefficients in decomposing polymer composites, *Porous Media, Mixtures and Multiphase Heat Transfer*, HTD-Vol. 117, pp. 51–60. ASME Winter Annual Meeting, San Francisco, California (December 1989).
8. J. Florio, Jr., An analytical and experimental investigation of the decomposition of glass-filled polymer composites, Ph.D. Dissertation, University of Rhode Island, Kingston, Rhode Island (1989).
9. J. Florio, Jr., J. B. Henderson and F. L. Test, Measurement of the thermochemical expansion of porous composite materials, *High Temp.–High Pressures* **21**, 157–165 (1989).
10. H. Ramamurthy, F. L. Test, J. Florio, Jr. and J.B. Henderson, Internal pressure and temperature distribution in decomposing polymer composites, *Proc. Ninth Heat Transfer Conf.*, Jerusalem, Israel (August 1990).
11. T. E. Wiecek, A study of the high temperature thermal response of decomposing and expanding polymer composites, M.S. Thesis, University of Rhode Island, Kingston, Rhode Island (1986).

ETUDE DES EFFETS DE L'HYPOTHESE DE L'EQUILIBRE THERMIQUE LOCAL SUR LA REPONSE GLOBALE THERMIQUE D'UN COMPOSITE POLYMERE DECOMPOSABLE AVEC BILLES DE VERRE

Résumé—Une étude analytique est faite pour déterminer la réponse thermique d'un composite polymère ablatif chargé de billes de verre. On utilise un nouveau modèle numérique, monodimensionnel, variable qui n'inclut pas l'hypothèse idéale d'un équilibre thermique local entre la matrice solide et les gaz de décomposition dans le réseau tortueux de pores du materiau. Les résultats de cette étude concernent la température du solide, celle des gaz de décomposition, la perte de masse du solide, la pression, la perméabilité, la porosité, le flux massique de gaz, le stockage de gaz, les profils du coefficient de dilatation volumétrique. On prédit des déviations par rapport à l'équilibre thermique local allant jusqu'à 200°C. Des pressions atteignant 10 atm sont prédites et l'existence de telles pressions élevées est vérifiée expérimentalement. Une étude des effets de l'hypothèse idéale de l'équilibre thermique local révèle des erreurs importantes.

UNTERSUCHUNGEN ÜBER DEN EINFLUSS EINES ANGENOMMENEN LOKALEN THERMISCHEN GLEICHGEWICHTS AUF DAS THERMISCHE VERHALTEN EINES SICH ZERSETZENDEN GLASFASERVERSTÄRKTEN POLYMERS

Zusammenfassung—Das thermische Verhalten eines gebräuchlichen, sich unter hohen Temperaturen zersetzenden, glasfaserverstärkten Polymers wird analytisch untersucht. Ein kürzlich entwickeltes, eindimensionales instationäres numerisches Modell wird verwendet, das auf die idealisierende Annahme eines lokalen thermischen Gleichgewichts zwischen der Feststoffmatrix und den in den Poren bei der Zersetzung entstehenden Gasen verzichtet. Folgende Größen werden berechnet: die Temperaturen von Feststoff und entstehenden Gasen, die Masse des sich zersetzenden Feststoffes, Druck, Permeabilität, Porosität, Massenstromdichte des Gases, gespeicherte Gasmasse, Expansion sowie die räumlichen Profile des Wärmeübergangskoeffizienten. Es werden Abweichungen vom örtlichen thermischen Gleichgewicht bis zu 200°C berechnet. Außerdem ergeben sich Drücke bis zu 10 atm—derartig hohe Drücke waren bereits früher in Versuchen festgestellt worden. Eine Untersuchung des Einflusses der idealisierenden Annahme vom lokalen thermischen Gleichgewicht zeigt, daß hieraus signifikante Fehler folgen.

ИССЛЕДОВАНИЕ ВЛИЯНИЯ ПРЕДПОЛОЖЕНИЯ О ЛОКАЛЬНОМ ТЕРМОДИНАМИЧЕСКОМ РАВНОВЕСИИ НА ТЕПЛОВУЮ РЕАКЦИЮ РАЗЛАГАЮЩЕГОСЯ ПОЛИМЕРНОГО СТЕКЛОНАПОЛНЕННОГО КОМПОЗИЦИОННОГО МАТЕРИАЛА

Аннотация—Проводится аналитическое исследование с целью определения тепловой реакции широко применяемого абляционного полимерного стеклонаполненного композита. При исследовании используется разработанная одномерная нестационарная численная модель без предположения о существовании локального термодинамического равновесия между матрицей твердого тела и газами, образующимися при раздожении внутри сложной пористой структуры материала. Получены результаты для температуры твердого тела, температуры образующегося при разложении газа, уноса массы твердого вещества, давления, проницаемости, пористости, массового потока газа, накопления массы газа, профилей коэффициентов теплового расширения и объемного теплопереноса. Предсказываются отклонения от локального термодинамического равновесия, составляющие 200°C. Предсказаны также значения давления вплоть до 10 атм, и получено экспериментальное подтверждение существования таких высоких давлений. Исследование влияния идеализированного предположения о локальном термодинамическом равновесии указывают на то, что оно может привести к существенным погрешностям.